



This is a repository copy of *Effect of a ring electrode on the cone-jet characteristics of ethanol in small-scale electro-spraying combustors*.

White Rose Research Online URL for this paper:
<http://eprints.whiterose.ac.uk/101244/>

Version: Accepted Version

Article:

Gan, Y., Zhang, X., Li, H. et al. (4 more authors) (2016) Effect of a ring electrode on the cone-jet characteristics of ethanol in small-scale electro-spraying combustors. *Journal of Aerosol Science*, 98. pp. 15-29. ISSN 0021-8502

<https://doi.org/10.1016/j.jaerosci.2016.05.001>

Article available under the terms of the CC-BY-NC-ND licence
(<https://creativecommons.org/licenses/by-nc-nd/4.0/>)

Reuse

This article is distributed under the terms of the Creative Commons Attribution-NonCommercial-NoDerivs (CC BY-NC-ND) licence. This licence only allows you to download this work and share it with others as long as you credit the authors, but you can't change the article in any way or use it commercially. More information and the full terms of the licence here: <https://creativecommons.org/licenses/>

Takedown

If you consider content in White Rose Research Online to be in breach of UK law, please notify us by emailing eprints@whiterose.ac.uk including the URL of the record and the reason for the withdrawal request.



eprints@whiterose.ac.uk
<https://eprints.whiterose.ac.uk/>

Effect of a ring electrode on the cone-jet characteristics of ethanol in small-scale electro-spraying combustors

Yunhua Gan^{a,b,*}, Xia Zhang^{a,b}, Haige Li^{a,b}, Yang Tong^{a,b}, Yang Zhang^c, Yanling Shi^d, Zeliang Yang^{a,b}

a. School of Electric Power, South China University of Technology, Guangzhou 510640, China;

b. Guangdong Province Key Laboratory of Efficient and Clean Energy Utilization, South China University of Technology, Guangzhou, 510640, China;

c. Department of Mechanical Engineering, The University of Sheffield, Sheffield, S1 3JD, UK;

d. Teaching and Training Center for Engineering Basis, South China Agricultural University, Guangzhou 510640, China;

Submitted for publication in

Journal of Aerosol Science

*Corresponding author: Prof. Yunhua Gan, Ph.D.,

Address: School of Electric Power, South China University of Technology, Wushan Road, Tianhe District, Guangzhou 510640, China

Tel/Fax: 00-86-20-87110613

Email: ganyh@scut.edu.cn.

Abstract

Two new micro-scale electro-spraying combustors of nozzle-grid and nozzle-ring-grid electrode configurations were designed. The experimental studies on the electro-spraying cone-jet characteristics in the micro-scale combustors were carried out using liquid ethanol as fuel. A digital camera was applied to visualize the electro-spraying at the cone-jet mode. The size and velocity distributions of the electro-spraying droplets were measured by a Phase Doppler Anemometer for both electrode configurations. Numerical calculation was performed to investigate the effects of the ring electrode on the electric field. A non-dimensional analysis was proposed to explain the liquid electro-spraying phenomena at the cone-jet mode. The results show that the electric field strength near the nozzle tip decreased when using the ring electrode with an appropriate voltage based on the superposition principle of the electric field, and the cone-jet mode could form at lower nozzle voltage without “satellite trapping”. Compared with the nozzle system without the ring electrode, the nozzle-ring system could produce smaller and more uniform droplets because of the more stable cone-jet mode. The lower velocity corresponded to the smaller droplet size, the velocity of the droplets was lower and the droplet size was smaller accordingly in the nozzle-ring system. It was found that the dimensionless droplet sizes in both the nozzle system and nozzle-ring system has a $1/2$ power dependence on dimensionless liquid flow rate.

Keywords: ring electrode; cone-jet mode; electro-spraying; droplet size; electric field strength distribution; non-dimensional analysis

Nomenclature

d	droplet diameter (mm)
d_{σ}	the corresponding jet diameter of the reference flow (mm)
d_{pred}	the droplet sizes predicted by the available correlations (mm)
d_{exp}	the droplet sizes measured in the experiments (mm)
d_n	inner diameter of nozzle (mm)
d_r	inner diameter of ring electrode (mm)
D_n	outer diameter of nozzle (mm)
D	outer diameter of grid (mm)
D_r	outer diameter of ring electrode (mm)
D_{mean}	arithmetic mean diameter (μm)
D_i	diameter of the individual particles (μm)
E_t	tangential electric field on the surface (V/m)
E_n°	outer normal electric field on the surface (V/m)
E_n^i	inner normal electric field on the surface (V/m)
K	electrical conductivity (S/m)
L	the distance between the nozzle tip and grid (mm)
L_1	the distance between nozzle tip and ring electrode (mm)
L_2	the distance between ring electrode and grid (mm)
M	the number of data points
N	total number of particles
p	pressure (Pa)

Δp	pressure jump over the interface from air to liquid (Pa)
Q	flow rate (ml/h)
Q_{σ}	the reference flow rate (ml/h)
r	radial coordinate (mm)
r_{σ}	the corresponding jet radius of the reference flow (mm)
r_s	cone-jet radius (mm)
δ	thickness of ring electrode (mm)
u	velocity component in the z direction (m/s)
u_{mean}	arithmetic mean axial velocity (m/s)
u_i	axial velocity of the individual particles (m/s)
v	velocity component in the r direction (m/s)
V_n	the voltage applied to nozzle (kV)
V_r	the voltage applied to ring electrode (kV)
V_{f1}	the volume fractions of liquid
V_{f2}	the volume fractions of air
z	axial coordinate (mm)

Greek symbols

α	reinitialization parameter
ε	dielectric constant of liquid
ε_r	relative permittivity
ε_0	dielectric constant of vacuum
ε_{ls}	parameter controlling the interface thickness (mm)

μ	dynamic viscosity (Pa·s)
ρ	fluid density (kg/m ³)
ρ_s	charge density along the surface (C/m ²)
ρ_v	the space charge density (C/m ³)
σ	gas-liquid surface tension (N/m)
τ	tangential shear stress (N)

1. Introduction

With the development of new technologies, more and more attention has been focused on the micro-power systems using micro-scale combustors (Cao & Xu, 2007; Gan et al., 2014; Mikami et al., 2013). The specific energy of liquid hydrocarbons is much higher than that of batteries. So, the liquid hydrocarbons-based micro-combustor can become competitive with the batteries (Chen et al., 2009; Xu et al., 2013). The liquid hydrocarbon must be evaporated and mixed with the air in premixed systems or injected directly in non-premixed systems, due to the large surface area to volume ratio in microchannels. The phase change from liquid to vapor in the microchannels occurs in an unstable way (Gan et al., 2015a). Recently, because the electro-spraying can produce monodisperse liquid droplets easily, motions of the charged droplets can be controlled by electric field (Gañán-Calvo, 1994; Gañán-Calvo, 2004; Gañán-Calvo and Montanero, 2009; Ghazian et al., 2014; Taylor, 1964), it has been adapted for liquid fuel injection (Agathou & Kyritsis, 2012). The injected liquid is supplied to a nozzle at a low flow rate, under an externally applied electric field,

and the electro-spraying is operated at typical modes (spindle mode, dripping mode, pulsating mode and cone-jet mode) (Li & Tok, 2008; Verdoold et al., 2014). At cone-jet mode, the interface between air and the liquid is charged to a high potential, the liquid meniscus becomes a stable cone, whose apex issues a narrow jet (Rezvanpour et al., 2012; Yan et al., 2003).

According to the scaling laws, the dimensionless electro-spray droplet size has a monotonic dependence on the $1/2$ power of the dimensionless liquid flow rate (Gañán-Calvo, 1994). Smaller droplets can be achieved at very low flow rate (Gañán-Calvo et al., 2013), the low throughput becomes the main drawback of the electro-spray system. In order to improve the throughput, many approaches have been considered (Holbrook et al., 2015; Li et al., 2014; Liu & Chen, 2014), which can be divided into three categories: multiplex, multi-jet and dual electrodes.

The electro-spray nozzles with very small diameters were used in the multiplex system, and the nozzle structures needed extra fabrication steps. The electro-spray sources were arranged in a hexagonal pattern which offers the highest packing density with a fixed distance between two neighboring nozzles (Oh et al., 2008). It was very important to obtain a uniform electric field. The nozzle diameter was very small to increase the throughput, or some dummy nozzles were introduced at the outmost region. So the device was complex and the nozzles might be plugged by the liquid easily.

The multi-jet mode operated with several jets issued around the tip of the nozzle, and some shape grooves were made at the tip of the nozzle to increase the electric

field around the nozzle tip (Kang et al., 2013). The multi-jet mode had much instability, and the liquid meniscus was in an unstable state, leading to a spread in droplet size and formation locations. The system required the sprays forming at the same time, and the geometry must be accurately reproduced from groove to groove.

A separation of the cone-jet region from the spraying region was generally desirable for stability and application considerations (Gan et al., 2015b). The dual electrodes spraying system consisted of a nozzle, a ring electrode, and a grounded grid was applied. An appropriate potential of the ring electrode should be selected to prevent the reversing of droplets paths. The spray passed through the ring electrode, and a stable cone-jet was established.

In present study, two different electro-spraying systems were compared to investigate the effect of the ring electrode on the cone-jet characteristics. The electro-spraying characteristics at cone-jet mode were visualized by a digital camera. The droplets size and velocity distributions were measured by a Phase Doppler Anemometer for both the electro-spraying systems. A numerical calculation was performed to investigate the effects of the ring electrode on the electric field. A non-dimensional analysis was carried out to explain the electro-spraying phenomena at cone-jet mode.

2. Experimental setup

2.1 The test rig

Fig.1 shows the test rig, which consisted of a liquid fuel feeding system, a test

section, a high voltage supply system and a droplet size and velocity measuring system. A capillary was used as a nozzle, and the fuel was supplied through a plastic tube to the nozzle by a syringe pump (KDS100, KD SCIENTIFIC) with an uncertainty of $\pm 1\%$. The nozzle was supported by a copper sleeve and a ceramic package. The different electro-spraying modes were visualized by a digital single-lens reflex camera (Canon EOS 5D Mark III) with a green laser light as an illuminating light source. The effective pixels are 22.3 million pixels, the highest resolution of the photos is 5760×3840 , the highest shutter speed is $1/8000$ s, ISO range is 100 to 25600. In present study, a setting of aperture at F 2.8, shutter speed at $1/2560$ s, and ISO at 800 was chosen. The liquid fuel was pure ethanol ($\text{CH}_3\text{CH}_2\text{OH}$, molecular weight of 46.07, purity $> 99.5\%$).

2.2 Test section

Two different of test sections with or without a ring electrode are illustrated in Fig.2. There were two electro-spraying systems: (1) nozzle system: the nozzle was maintained at high potential by connecting it to a direct-current (DC) power source, and the stainless steel grid was grounded; (2) nozzle-ring system: the nozzle and the ring electrode were connected to two DC power source separately, and the stainless steel grid was also grounded.

The inner and outer diameters of the stainless steel nozzle were 0.9 mm and 1.2 mm respectively ($d_n=0.9$ mm, $D_n=1.2$ mm). The length of protruding section of the nozzle was 1.5 mm ($h= 1.5$ mm). The inner and outer diameters of the ring electrode were 12.4 mm and 16 mm respectively ($d_r=12.4$ mm, $D_r=16$ mm), its thickness was

5mm ($\delta=5$ mm). The stainless steel grid had a diameter of $D=16$ mm, and each hole in it had a diameter of 1 mm. A high DC power source (Model DW-P103-1AC) was used to supply high voltage on the nozzle (V_n). For the nozzle system, the stainless steel grid was arranged above the tip of the nozzle with a vertical distance of $L=26.1$ mm. For the nozzle-ring system, the ring electrode was arranged above the tip of the nozzle with a distance of $L_1=1.1$ mm. Another DC power source (Model 71030P) was used to supply high voltage on the ring electrode (V_r). The stainless steel grid was arranged above the ring electrode with a distance of $L_2=20$ mm.

2.3 Droplet size and velocity measurement

A Phase Doppler Anemometer (PDA) (Dantec Dynamics classic PDA) was used to measure the sizes of the droplets (Li et al., 2013). The PDA system included a fiber optic probe, a signal processor, a receiver probe and an argon-ion laser. Droplet distributions at different spatial locations were measured by adjusting a three dimensional auto control coordinate system with a dimension of 560×560×580 mm. An argon-ion laser generator and optical splitter were used to generate two laser beams with a spacing of 40 mm. The wavelength was 514.5 nm for beam U1 (green) and 488 nm for beam U2 (blue). The beam diameters were 1.35 mm and beam expander ratios were set to 1. The shift frequency of one of the two beams is 40 MHz. The fringe spacing was 6.87 μm and 6.51 μm for U1 and U2, respectively, fringes moved in a negative direction. A dedicated electronic processor sampled and analyzed the signal using BSA Flow Software. The spherical validation band was set to 10% to ensure a high sphericity of recorded droplets and a high accuracy of droplet size. The

sample number at every measuring position was set to 2000 and sampling time was 10 s which enable estimation of droplet size and velocity statistics with confidence. Droplets size was measured from the phase difference between the quasi-periodic signals collected by two appropriately positioned detectors. An automatic check rejects signals emitted from non-spherical drops. Other signals from droplets crossing the measuring volume far from its center were rejected because the linear relationship between droplet diameter and phase shift ceases to be valid for those cases. The intersection of the two beams was located as near to the axis (Gañán-Calvo, 1997). After comparing the droplet size distribution at the different cross sections, measurements were performed at the section ($z=10$ mm) up the tip of the nozzle, and size distribution was determined based on 17 points. Fig.3 shows the distribution of measuring points, which distribute on the concentric circles of different radiuses.

2.4 Error Analysis

In present study, ethanol was used as the liquid fuel and its physical properties at 25 °C are shown in Table 1. The experiment was conducted in the following variation ranges of operating parameters: liquid ethanol flow rate Q of 0.2-4 ml/h, applied voltage on the nozzle electrode V_n of 0-6.8 kV, the applied voltage on the ring electrode V_r was 1 kV, the distance L_1 was 1.1 mm, the distance L_2 was 20 mm, the distance L was 26.1 mm. The measurement errors of a set of parameters are listed in Table 2.

3. Numerical simulation

3.1 Modeling Methodology

The liquid was supplied into a nozzle at a very low flow rate. A stable cone-jet mode can be formed under an externally applied electric field. Then the liquid ethanol was broken into small droplets, which passed through the ring electrode and then gathered on the stainless steel grid. The geometric model of numerical simulation is shown in Fig.4. The region between the nozzle and the ring electrode was named as the cone-jet region, and the space between the ring electrode and the grid was named as the spraying region.

The liquid flow would change the electric field distribution around the nozzle. Thus, the electric field distribution needed to be solved for the whole region (Lim et al, 2011). The governing equations for both fluid and electric field were solved for the cone-jet region. To track the liquid-gas interface, the level set method had been incorporated into the simulations using a software package Fem-Lab (Comsol). The coupling simulation area was $0 \text{ mm} \leq r \leq 8 \text{ mm}$, $-5 \text{ mm} \leq z \leq 26.1 \text{ mm}$, the electric field simulation area was $0 \text{ mm} \leq r \leq 50 \text{ mm}$, $-30 \text{ mm} \leq z \leq 70 \text{ mm}$. Two-dimensional axisymmetric calculation model and free triangular mesh were used. A steady-state solver was adopted in the calculation process. A normal element size was used in present simulation. In order to check the effect of mesh size on the numerical results, three mesh sizes were considered. The first one was 1256 domain units and 463 boundary elements, the second was 1500 domain units and 500 boundary elements, the third was 900 domain units and 400 boundary elements. The numerical results did not vary significantly with the mesh size, thus the first element size mentioned above

was used in present simulation.

3.2 Governing equations

The governing equations were solved in the cone-jet region to obtain the details of fluid flow and its interaction with the electric field. Additional body forces were added to the Navier-Stokes equations for considering the surface tension (\mathbf{F}_{st}) and electric stress (\mathbf{F}_{es}) (Ghazian et al., 2014).

$$\nabla \cdot \mathbf{u} = 0 \quad (1)$$

$$\rho \frac{\partial \mathbf{u}}{\partial t} + \rho(\mathbf{u} \cdot \nabla)\mathbf{u} - \nabla \cdot [-p\mathbf{I} + \mu(\nabla\mathbf{u} + (\nabla\mathbf{u})^T)] = \rho\mathbf{g} + \mathbf{F}_{st} + \mathbf{F}_{es} \quad (2)$$

where \mathbf{u} denotes fluid velocity, ρ is the fluid density, \mathbf{g} is the gravitational acceleration, μ is the dynamic viscosity, \mathbf{I} is the 3×3 identity matrix, and p is the pressure.

To obtain the electric field distribution, the Poisson's equation for the electrical potential was expressed as follows:

$$\nabla \cdot \mathbf{D} = \rho_v \quad (3)$$

$$\mathbf{E} = -\nabla V \quad (4)$$

$$\mathbf{D} = \varepsilon\mathbf{E} \quad (5)$$

Where \mathbf{D} is the electric displacement, \mathbf{E} is the electric field intensity, V is the voltage, ε is the dielectric constant of the liquid, ρ_v is the space charge density.

The electric stress could be calculated by taking the divergence of the Maxwell stress tensor, neglecting the effect of magnetic field, the Maxwell stress tensor could be defined as follows:

$$\mathbf{TM}_{ij} = \varepsilon_r \varepsilon_0 \mathbf{E}_i \mathbf{E}_j - \frac{1}{2} (\varepsilon_r \varepsilon_0 \mathbf{E}^2) \delta_{ij} \quad (6)$$

$$\mathbf{F}_{es} = \nabla \cdot \mathbf{TM} \quad (7)$$

$$\varepsilon_r = \varepsilon_{r1}V_{f1} + \varepsilon_{r2}V_{f2} \quad (8)$$

where ε_r is the relative permittivity, ε_0 is the dielectric constant of vacuum, E_i , E_j is the electric field component in the i , j direction, $i=j$, $\delta_{ij}=1$, or $\delta_{ij}=0$. ε_{r1} and ε_{r2} denote the relative permittivity of liquid and air, V_{f1} and V_{f2} are the volume fractions of each fluid, respectively. Although the relative permittivity of liquid and air are constant, the volume fractions of each fluid changed with the interface between the liquid and air, the relative permittivity ε_r changed during the numerical simulation.

The level set method described the evolution of the interface between the liquid and air tracing an iso-potential curve of the level set function (φ). The function φ is governed by:

$$\frac{\partial \varphi}{\partial t} + \nabla \cdot (\varphi \mathbf{u}) = \alpha \nabla \cdot \left[\varepsilon_{ls} \nabla \varphi - \varphi (1 - \varphi) \frac{\nabla \varphi}{|\nabla \varphi|} \right] \quad (9)$$

Where ε_{ls} is the parameter controlling the interface thickness, α is the reinitialization parameter.

3.3 Boundary conditions

The fluid-air interface was affected by the electrostatic field force and the surface tension. The effect of fluid viscous force was ignored. The force balance was reached under the proper voltage, and a stable cone jet atomization model was obtained. The boundary conditions for the hydrodynamic equations were listed as follows (Yan et al., 2003).

At the inlet of the nozzle:

$$z = -h$$

$$u = \frac{4Q}{\pi d_n^2}, v = 0 \quad (10)$$

At the tip of the nozzle:

$$z=0, 0 \leq r \leq r_s$$

$$u = \frac{Q}{\pi r^2}, v = 0 \quad (11)$$

Along the axis:

$$r=0, -h \leq z \leq L_1 + L_2$$

$$\frac{\partial u}{\partial r} = 0, \frac{\partial v}{\partial r} = 0, v = 0 \quad (12)$$

Along the liquid-air interface:

$$r=r_s, -h \leq z \leq L_1 + L_2$$

$$\boldsymbol{\tau} = \rho_s \cdot \mathbf{E}_t \quad (13)$$

$$\Delta p = \sigma \left(\frac{1}{r_1} - \frac{1}{r_2} \right) - \frac{\varepsilon_0}{2} \left[E_n^{o2} - \varepsilon_r E_n^{i2} + (\varepsilon_r - 1) E_t^2 \right] \quad (14)$$

where u, v is the velocity component in the z, r directions, r_s is the cone-jet radius, Q is the liquid flow rate, d_n is the inner diameter of nozzle, ρ_s is the charge density along the surface, ε_r is the relative permittivity, ε_0 is the dielectric constant of vacuum, $\boldsymbol{\tau}$ and \mathbf{E}_t are the tangential shear stress and tangential electric field on the surface, respectively. E_n^o, E_n^i is the outer and inner normal electric field on the surface, σ is the surface tension, r_1, r_2 is the inner and outer radii of curvature of the free surface, Δp is the pressure jump over the interface from air to liquid.

3.4 Numerical implementation and model verification

Two levels of the numerical procedures were adopted in this simulation, an outer loop of electric potential field in the whole region and an inner loop for cone-jet simulation in cone-jet region. The procedures are listed below.

- (1) Both the cone-jet region and spraying region were used for the initial electric

field simulation using Eqs. (3) - (5), no liquid presented in it.

- (2) The data from the electric field simulation for the whole region was extracted and applied to cone-jet region as the boundary conditions of the electrical field.
- (3) The cone-jet simulation was carried out using Eqs. (1), (2) and (9).
- (4) Once a cone-jet was obtained, a new electric field simulation would be carried out again, because the relative permittivity ϵ_r changed.
- (5) The electrical field simulation in the whole region was checked for convergence by comparing the electrical field applied to the cone-jet region with the new electric field distribution in step (4). If convergence was reached, the simulation finished, or steps (2)-(5) were repeated.

When the flow rate was 1 ml/h, and the applied voltage on the ring electrode V_r was 1 kV, the nozzle voltage V_n was 4.19 kV, the semi-cone angle simulated by Comsol was 37.3° , that measured in the experiments was 38.1° , a good agreement with them was obtained, and the accuracy of the simulation was well verified.

4 Results and discussions

4.1 The electric field distributions

The electrical potential distribution in the absence of the liquid was calculated based on the Poisson's equation. The electrical potential distribution with the liquid was simulated by using the relative permittivity ϵ_r as described in the Eqs. (8). The electric field distribution could be obtained through calculating the electrical potential

distribution. The results of the numerical simulation using software (Comsol) are shown in Fig.5 and Fig.6.

Fig.5 (a) shows the electrical field distribution near the nozzle tip without liquid at the cone-jet region ($z= 0$ mm) for the two electro-spraying systems. According to the superposition principle, the electric field strength in the nozzle-ring system was smaller than that in the nozzle system. Both of the electric field of the two systems was higher than the breakdown limit of air (3×10^6 V/m). When the voltage was applied to the electrode, ambient discharge formed near the nozzle tip, generating an audible noise.

Fig. 5(b) shows the electrical field distribution without the liquid at the spraying region ($z=5$ mm, 10mm, 20mm) for the two electro-spraying systems. For the nozzle system, the electric field strength ($z=5$ mm) decreased rapidly with the increasing of the radius r . For the nozzle-ring system, the section of $z=5$ mm was in the ring electrode, the electric field strength was zero ($6.2\text{mm}<r<8\text{mm}$) because of the ring electrode. For both nozzle system and nozzle-ring system, the electric field distribution ($z=10$ mm, 20mm) became more uniform with the increasing of the radius r . The electric field strength decreased with the increasing of the axial coordinate z , and the electric field strength near the grid ($z=20$ mm) increased because of the reverse electric field. As mentioned above in section 2.3, the experimental measurements of droplet sizes performed at $z=10$ mm were acceptable to identify the difference between the two systems.

Fig.6 (a) shows the electrical field distribution near the nozzle tip with liquid at

the cone-jet region ($z=0$ mm) for the two electro-spraying systems. Both of the electric field of the two systems was lower than the breakdown limit of air (3×10^6 V/m), the experiments were performed without ambient discharge. For the nozzle-ring system, the electric field near the nozzle tip decreased due to the effect of the ring electrode. The rapid increment was reduced in the electric field near the cone-tip, and the sudden changes were prevented. Thus, a more stable cone-jet formed.

Fig.6 (b) shows the electrical field distribution with the liquid at the spraying region ($z=5$ mm, 10mm, 20mm) for the two electro-spraying systems. Comparing with the nozzle system, the electric field strength was much lower in the nozzle-ring system. The electric field between the ring electrode and the ground electrode supplied the driving force for the movement of the droplets. If the ring electrode voltage was too low, the satellite droplets were driven out from the shield of the spraying core. They would reverse their paths and flowed back to the ring electrode, causing flooding and finally interruption of the flow. This phenomenon was called “satellite trapping” (Deng & Gomez, 2007), which should be prevented. For the nozzle-ring system, the electric field strength was suitable to drive the droplets to the grounded electrode without “satellite trapping”.

4.2 The cone-jet mode

Fig.7 shows the photos of electro-spraying at cone-jet mode obtained by a digital camera. The experiments were carried out at the fixed flow rate of 1.0ml/h. Some different electro-spraying modes were observed along with the increasing of the nozzle voltage V_n . At the cone-jet mode, the interface between air and the liquid was

charged to a high potential, the liquid meniscus became a stable cone, whose apex issued a narrow jet. For the nozzle system, the distance between the stainless steel grid and the nozzle tip L was 26.1 mm, the stable cone-jet mode was observed when the nozzle voltage V_n ranged from 5 to 5.5 kV. Fig.7 (a) is the photo of electro-spraying at cone-jet mode when $V_n=5.2$ kV. For the nozzle-ring system, the distance between the nozzle tip and the ring electrode L_1 was 1.1 mm, the distance between the ring electrode and the stainless steel grid L_2 was 20 mm. The applied voltage on the ring electrode V_r was 1 kV. The stable cone-jet mode was observed when the nozzle voltage V_n ranged from 4.1 to 4.6 kV. Fig.7 (b) is the photo of electro-spraying at cone-jet mode when $V_n=4.2$ kV.

For the nozzle system, a high voltage was applied to the nozzle to form a strong electric field. The cone-jet was obtained when the electric field strength exceeded the critical value. And if the voltage was too high, the strong electric field may destabilize the cone and the spraying.

For the nozzle-ring system, the spraying passed through the ring electrode. The electric field near the nozzle tip decreased due to the effect of the ring electrode. The rapid increment was reduced in the electric field near the cone-tip and the sudden changes were prevented, so the ring electrode shielded the cone-jet region, the stable cone-jet mode can be achieved at the lower nozzle voltage. If the ring electrode V_r was too low, the “satellite trapping” phenomenon described in section 4.2 appeared. The satellite droplets were trapped by the ring electrode and thus they couldn't reach the ground electrode completely. On the other hand, if the ring electrode V_r was too

high, the stable cone-jet would be obtained at higher nozzle voltage, which was unnecessary.

4.3 Droplet size and velocity at four different modes

Fig.8 shows the influence of the nozzle voltage V_n on the droplet size and velocity for the nozzle system at the flow rate of 1.0 ml/h. The distance between the stainless steel grid and the nozzle tip L was 26.1 mm. The measurements were performed at the position of $z=10$ mm. The arithmetic mean diameter can be defined as follows:

$$D_{\text{mean}} = \frac{1}{N} \sum_{i=1}^N D_i \quad (15)$$

Where N is the total number of particles, D_i is the diameter of the individual particles.

The arithmetic mean axial velocity can be defined as follows:

$$u_{\text{mean}} = \frac{1}{N} \sum_{i=1}^N u_i \quad (16)$$

Where N is the total number of particles, u_i is the axial velocity of the individual particles.

Fig.8 shows the average diameters and velocity of the droplets at different positions which were described in Fig.3. Fig.8 (a) shows the average diameters of the droplets for nozzle system at different modes and positions. As the nozzle voltage V_n increased from 4.3 kV to 5 kV (at pulse-jet mode), the droplet sizes decreased from 25 μm to 13 μm , and the droplet sizes were nonuniform at different positions. When V_n increased from 5 to 5.5 kV (at cone-jet mode), nearly monodisperse droplets appeared with the average sizes of around 12 μm . If V_n exceeded 5.5 kV (at skewed cone-jet or

multi-jet modes), the droplet sizes became nonuniform. Fig.8 (b) shows the average axial velocity of the droplets for nozzle system at different modes and positions. The droplets at positions 0-8 which were described in Fig.3 were close to the axis of the core (central area). The lower velocity corresponded to the smaller droplet, and the more uniform velocity corresponded to the more uniform droplet size. But for the droplets which were far away from the center (satellite area), droplets size and velocity had no obvious regularity, due to the effect of other forces, such as the coulomb force.

Fig.9 shows the influence of the nozzle voltage V_n on the droplet sizes and velocity for the nozzle-ring system at the flow rate of 1.0 ml/h. The distance between the nozzle tip and the ring electrode L_1 was 1.1 mm, the distance between the ring electrode and the stainless steel grid L_2 was 20 mm, and the applied voltage on the ring electrode V_r was 1.0 kV. The measurements were performed at the position of $z=10\text{mm}$. Fig.9 (a) shows the average diameters of the droplets for nozzle system at different modes and positions. When V_n ranged from 4.1 to 4.6 kV (at cone-jet mode), nearly monodisperse droplets appeared with the average sizes of around 9 μm . Fig. 9(b) shows the average velocity of the droplets at different modes and positions. The change trend of the droplets size and velocity were the same as that described in the nozzle system. But the velocity was lower than that in the nozzle system, and the corresponding droplet size was smaller too.

Comparing with the nozzle system, smaller and more uniform droplets were found in the nozzle-ring system at the cone-jet mode and the same flow rate. The

droplets breakup process was dominated by the axisymmetric disturbance. For the nozzle-ring system, the axisymmetric disturbance was protected by the ring electrode, due to the decreasing of the electric field strength neat the cone-tip. Thus, the cone was more stable and produced smaller and more uniform droplets.

4.4 The scaling law

4.4.1 Non-dimensional analysis

The scaling law for droplet sizes is a function of the parameters governing the problem. The droplet diameter d depends on the liquid properties (density ρ and viscosity μ , electrical conductivity K , gas-liquid surface tension σ , and relative permittivity ϵ_r) as well as the flow rate Q , nozzle voltage V_n , ring voltage V_r , vacuum permittivity ϵ_0 , and a given geometrical configuration. For the electro-spraying at the cone-jet mode, the droplet sizes keep constant as the voltage changes, so the influence of the voltage can be negligible. The relationship between droplet sizes and flow rate was developed by Gañán-Calvo (Gañán-Calvo et al., 2009).

$$\frac{r_d}{(\rho Q^2/\Delta P)^{1/4}} = k_d \quad (17)$$

$$\Delta p = k_p \left(\frac{\sigma^2 K^2 \rho}{\epsilon_0^2} \right)^{1/3} \quad (18)$$

Where r_d is the radius of the resulting droplets, ρ is the density of the liquid, Q is the volume flow rate of the liquid, Δp is the pressure jump caused by the Maxwell stresses and surface tension, k_d is a nearly universal constant, k_p is a constant of order unity, ϵ_0 is the permittivity of a vacuum, σ is the gas-liquid surface tension, K is the electrical conductivity of the liquid.

The reference flow rate and the corresponding jet radius were defined as follows:

$$Q_{\sigma} = \left(\frac{\sigma^4}{\rho \Delta p^3} \right)^{1/2} \quad (19)$$

$$r_{\sigma} = \frac{\sigma}{\Delta p} \quad (20)$$

When Eqs.(19) and (20) were put into Eq.(17), it can be obtained as follows:

$$\frac{d}{d_{\sigma}} = k_d \left(\frac{Q}{Q_{\sigma}} \right)^{1/2} \quad (21)$$

Where d is the diameter of the resulting droplets, d_{σ} is the corresponding jet diameter of the reference flow rate, Q_{σ} is the reference flow rate.

The scaling law Eq.(21) shows the relationship between the dimensionless diameter d/d_{σ} and a function of the dimensionless flow rate Q/Q_{σ} .

4.4.2 Droplet size scaling law

The droplet sizes were measured at cone-jet mode both for the nozzle system and the nozzle-ring system. The droplet size distributions of these two different electro-spraying systems are shown in the Fig.8 and Fig.9. The droplet size distributions at cone-jet mode were uniform at various positions, so the droplets measured could be considered as nearly monodisperse. In present study, the arithmetic mean diameter D_{mean} was chosen as the droplet diameter d . Fig.10 shows the dimensionless diameter d/d_{σ} as a function of the dimensionless flow rate Q/Q_{σ} . The dimensionless droplet sizes in both nozzle system and nozzle-ring system were found to obey the scaling law as dimensionless flow rate. Base on the present experimental results, the values of k_d were fitted. For the nozzle system, $k_d=0.75$; and for the nozzle-ring system, $k_d=0.50$.

The predictive capability of these correlations was overall evaluated by the mean

relative error (MRE), defined as

$$\text{MRE} = \frac{1}{M} \sum \frac{|d_{\text{pred}} - d_{\text{exp}}|}{d_{\text{exp}}} \times 100\% \quad (22)$$

where M is the number of data points, d_{pred} is the droplet sizes predicted by the available correlations, d_{exp} is the droplet sizes measured in the experiments. Based on present experimental results, the fitted equation (23) had a MRE of 14.3%, and the fitted equation (24) had a MRE of 25.2%.

$$\frac{d}{d_{\sigma}} = 0.75 \left(\frac{Q}{Q_{\sigma}} \right)^{1/2}, \quad \text{for the nozzle system (23)}$$

$$\frac{d}{d_{\sigma}} = 0.50 \left(\frac{Q}{Q_{\sigma}} \right)^{1/2}, \quad \text{for the nozzle-ring system (24)}$$

5 Conclusions

In present study, two different micro-combustors were designed, and some experiments on electro-spraying in the combustors using liquid ethanol as fuel were carried out. The droplet size and velocity distributions were measured by PDA at different electro-spraying modes. The electric field distributions were numerically calculated at the cone-jet mode. And the non-dimensional analysis was performed based on the scaling law at the cone-jet mode. Some main conclusions can be achieved as following:

- (1) The electric field strength near the nozzle tip in the nozzle-ring system at cone-jet mode and the same flow rate was smaller than that for the nozzle system according to the superposition principle of electric field.
- (2) The rapid increment was reduced in the electric field near the cone-tip and the sudden changes were prevented, a more stable cone-jet mode was obtained in the nozzle-ring system.

- (3) Comparing with the nozzle system, the nozzle-ring electro-spraying system could produce smaller and more uniform droplets with lower velocity because of the more stable cone-jet mode.
- (4) It was found that the dimensionless droplet sizes in both the nozzle system and nozzle-ring system has a $1/2$ power dependence on dimensionless liquid flow rate.

Acknowledgements

The authors gratefully acknowledge the National Nature Science Foundation of China (51376066, 5151101381), State Key Laboratory of Engines, Tianjin University (K2016-01), Project on the Integration of Industry, Education and Research from Guangdong Province and the Ministry of Education (2012B09100156) and the Central Universities Fundamental Research Project in South China University of Technology (201522083).

References

- Agathou, M. S., & Kyritsis, D. C. (2012). Electrostatic atomization of hydrocarbon fuels and bio-alcohols for engine applications. *Energy Conversion and Management*, 60, 10-17.
- Cao, H. L., & Xu, J. L. (2007). Thermal performance of a micro-combustor for micro-gas turbine system. *Energy Conversion and Management*, 48, 1569-1578.
- Chen, J., Peng, X. F., Yang, Z. L., & Cheng, J. (2009). Characteristics of liquid

ethanol diffusion flames from mini tube nozzles. *Combustion and Flame*, 156, 460-466.

Deng, W. W., & Gomez, A. (2007). Influence of space charge on the scale-up of multiplexed electrosprays. *Journal of Aerosol Science*, 38, 1062-1078.

Gan, Y. H., Xu, J. L., Yan, Y. Y., Wang, M., Luo, Y. L., & Yang, Z. L. (2014). A comparative study on free jet and confined jet diffusion flames of liquid ethanol from small nozzles. *Combustion Science and Technology*, 186, 120-138.

Gan, Y. H., Luo, Y. L., Wang, M., Shi, Y. L., & Yan, Y. Y. (2015a). Effect of alternating electric fields on the behaviour of small-scale laminar diffusion flames. *Applied Thermal Engineering*, 89, 306-315.

Gan, Y. H., Luo, Z. B., Cheng, Y. P., & Xu, J. L. (2015b). The electro-spraying characteristics of ethanol for application in a small-scale combustor under combined electric field. *Applied Thermal Engineering*, 87, 595-604.

Gañán-Calvo, A. M., Lasheras, J. C., Davila, J., & Barrero, A. (1994). The electrostatic spray emitted from an electrified conical meniscus. *Journal of Aerosol Science*, 25, 1121-1142.

Gañán-Calvo, A. M., Davila, J., & Barrero, A. (1997). Current and droplet size in the electrospraying of liquids. Scaling laws. *Journal of Aerosol Science*, 28, 249-275.

Gañán-Calvo, A. M. (2004). On the general scaling theory for electrospraying. *Journal of Fluid Mechanics*, 507, 203-212a.

Gañán-Calvo, A. M., & Montanero, J. M. (2009). Revision of capillary cone-jet physics: Electrospray and flow focusing. *Physical Review E*, 79, 066305.

- Gañán-Calvo, A. M., Rebollo-Munoz, N., & Montanero, J. M. (2013). The minimum or natural rate of flow and droplet size ejected by Taylor cone-jets: Physical symmetries and scaling laws. *New Journal of Physics*, 15, 033035.
- Ghazian, O., Adamiak, K., & Castle, G. S. P. (2014). Spreading and retraction control of charged dielectric droplets. *Colloids and Surfaces a-Physicochemical and Engineering Aspects*, 448, 23-33.
- Holbrook, L., Hindle, M., & Longest, P. W. (2015). Generating charged pharmaceutical aerosols intended to improve targeted drug delivery in ventilated infants. *Journal of Aerosol Science*, 88, 35-47.
- Kang, J. S., Park, I., Jung, J. H., & Kim, S. S. (2013). Free-surface electrospray technique using a multi-hole array. *Journal of Aerosol Science*, 55, 25-30.
- Li, C., Chang, M., Yang, W. W., Madden, A., & Deng, W. W. (2014). Ballpoint pen tips as robust cone-jet electrospray emitters. *Journal of Aerosol Science*, 77, 10-15.
- Li, J. L., & Tok, A. (2008). Electrospraying of water in the cone-jet mode in air at atmospheric pressure. *International Journal of Mass Spectrometry*, 272, 199-203.
- Li, Z. H., Wu, Y. X., Yang, H. R., Cai, C. R., Zhang, H., Hashiguchi, K., Takeno, K., & Lu, J. F. (2013). Effect of liquid viscosity on atomization in an internal-mixing twin-fluid atomizer. *Fuel*, 103, 486-494.
- Lim, L. K., Hua, J., Wang, C. H., & Smith, K. A. (2011). Numerical simulation of cone-jet formation in electrohydrodynamic atomization. *AIChE Journal*, 57, 57-78.
- Liu, Q. L., & Chen, D. R. (2014). An electrospray aerosol generator with x-ray photoionizer for particle charge reduction. *Journal of Aerosol Science*, 76, 148-162.

- Mikami, M., Maeda, Y., Matsui, K., Seo, T., & Yuliati, L. (2013). Combustion of gaseous and liquid fuels in meso-scale tubes with wire mesh. *Proceedings of the Combustion Institute*, 34, 3387-3394.
- Oh, H., Kim, K., & Kim, S. (2008). Characterization of deposition patterns produced by twin-nozzle electrospray. *Journal of Aerosol Science*, 39, 801-813.
- Rezvanpour, A., Lim, E. W. C., & Wang, C. H. (2012). Computational and experimental studies of electrohydrodynamic atomization for pharmaceutical particle fabrication. *AIChE Journal*, 58, 3329-3340.
- Taylor, G. (1964). Disintegration of water drops in an electric field. *Proceedings of the Royal Society A: Mathematical, Physical and Engineering Sciences*, 280, 383-397.
- Verdoold, S., Agostinho, L. L. F., Yurteri, C. U., & Marijnissen, J. C. M. (2014). A generic electrospray classification. *Journal of Aerosol Science*, 67, 87-103.
- Xu, T., Gao, X. N., Yang, J., Gan, Y. H., Yang, Z. L., & Zhang, Z. G. (2013). Experimental and numerical simulation study of the microscale laminar flow diffusion combustion of liquid ethanol. *Industrial & Engineering Chemistry Research*, 52, 8021-8027.
- Yan, F., Farouk, B., & Ko, F. (2003). Numerical modeling of an electrostatically driven liquid meniscus in the cone-jet mode. *Journal of Aerosol Science*, 34, 99-116.

Table captions

Table 1 Physical properties of ethanol (25⁰C)

Table 2 Error analysis

Table 1 Physical properties of ethanol (25⁰C)

Density	Viscosity	Surface tension	Conductivity	Relative permittivity
kg/m ³	Pa·s	N/m	S/m	—
789.3	1.07×10 ⁻³	0.022	5.1×10 ⁻⁵	25.3

Table 2 Error analysis

Parameters	Measure tool	Ranges	Error
Flow rate, Q	Syringe pump	0-4 ml/h	$\pm 1.0\%$
Voltage, V_n	DC power supply	0-2 kV	$\pm 1.0\%$
Voltage, V_r	DC power supply	0-7 kV	$\pm 1.0\%$
Diameter, d_n, D_n, d_r, D_r, D	Vernier caliper	0.9-16 mm	± 0.02 mm
Thickness of ring electrode, δ	Vernier caliper	5 mm	± 0.02 mm
Droplet size	PDA	0-250 μm	$\pm 1.0\%$
Droplet velocity	PDA	0-50 m/s	$\pm 1.0\%$

Figure captions

Fig.1 Schematic diagram of the test rig

Fig.2 Electro-spraying systems (a) nozzle system; (b) nozzle-ring system

Fig.3 Distribution of measurement points using PDA

Fig.4 Geometric model of numerical simulation

Fig.5 Electric field distributions at cone-jet region and spraying region without fuel

(a) at the cone-jet region; (b) at the spraying region

Fig.6 Electric field distributions at cone-jet region and spraying region with fuel

(a) at the cone-jet region; (b) at the spraying region

Fig.7 Typical images of the electro-spraying in the two different systems

(a) nozzle system ($L=26.1$ mm, $V_n=5.2$ kV, $Q=1.0$ ml/h)

(b) nozzle-ring system ($L_1=1.1$ mm, $L_2=20$ mm, $V_n=4.2$ kV, $V_r=1$ kV, $Q=1.0$ ml/h)

Fig.8 Droplet size and velocity distributions for nozzle system at different modes and positions ($L=26.1$ mm, $z=10$ mm, $Q=1$ ml/h)

(a) Droplet size distribution for nozzle system at different modes and positions

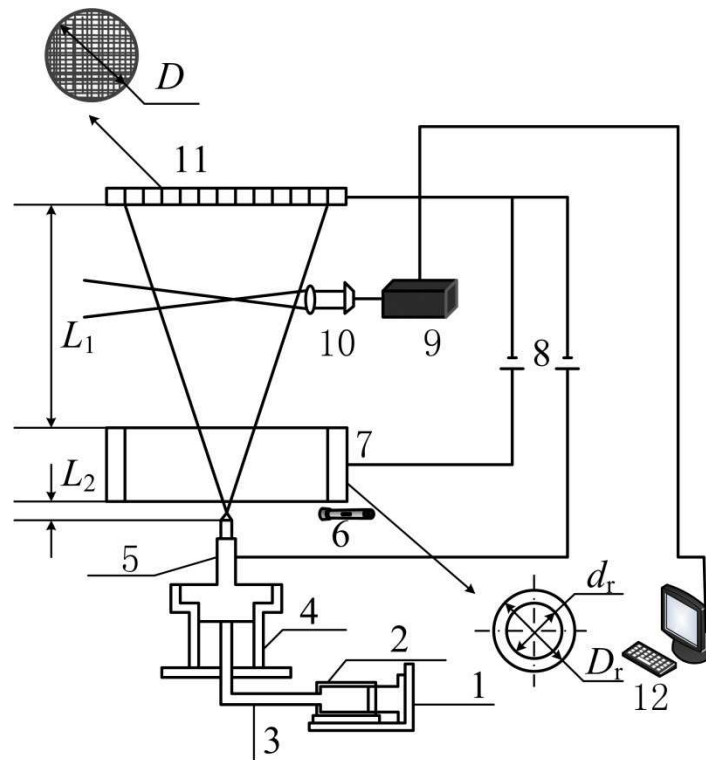
(b) Droplet velocity distribution for nozzle system at different modes and positions

Fig.9 Droplet size and velocity distributions for nozzle-ring system at different modes and positions ($L_1=1.1$ mm, $L_2=20$ mm, $z=10$ mm, $V_2=1$ kV, $Q=1$ ml/h)

(a) Droplet size distribution for nozzle-ring system at different modes and positions

(b) Droplet velocity distribution for nozzle-ring system at different modes and positions

Fig.10 Dimensionless average droplet size versus dimensionless average flow rate at cone-jet mode



1- syringe pump; 2- syringe; 3- plastic pipe; 4- substrate; 5- nozzle; 6- laser lamp;
 7- ring electrode; 8- high-voltage DC power supply; 9- laser; 10-focusing lens; 11-
 steel grid; 12-computer;

Fig.1 Schematic diagram of the test rig

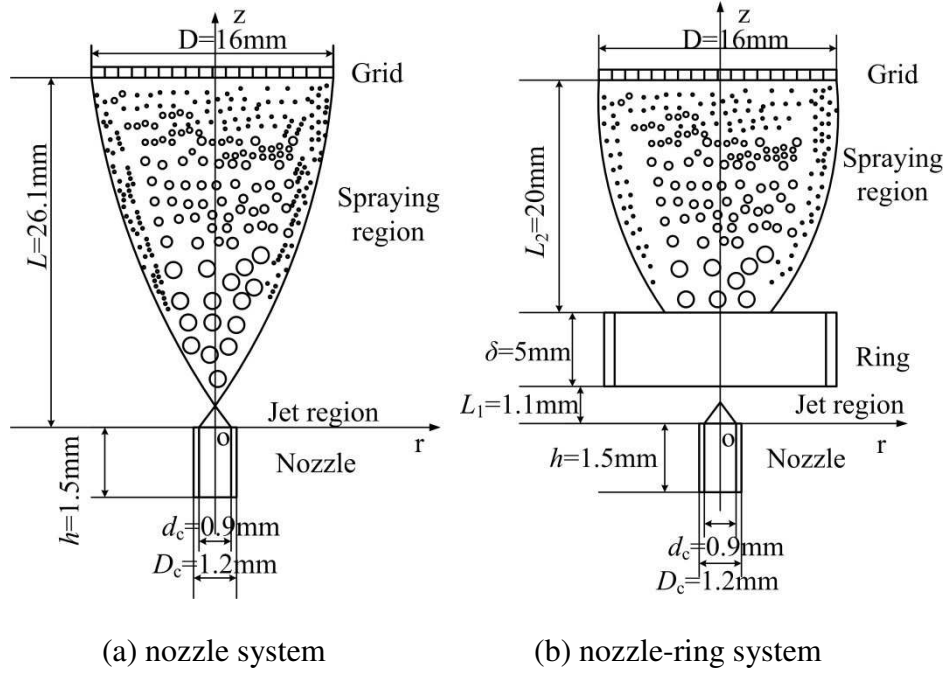


Fig.2 Electro-spraying systems with or without a ring electrode

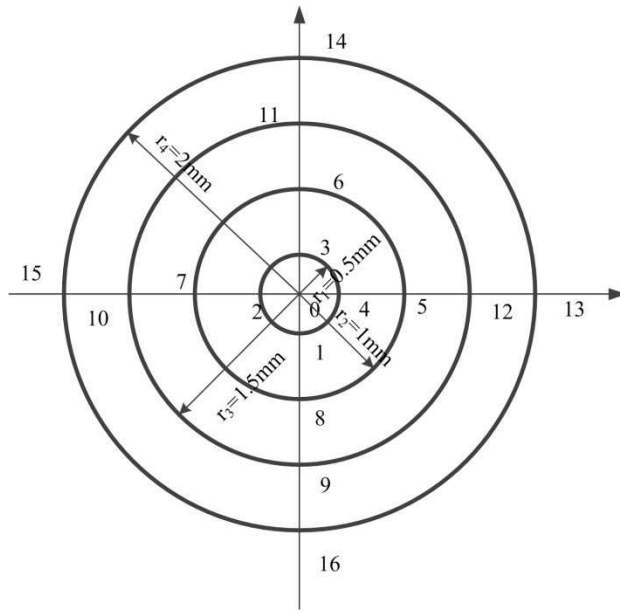


Fig.3 Distribution of measurement points using PDA

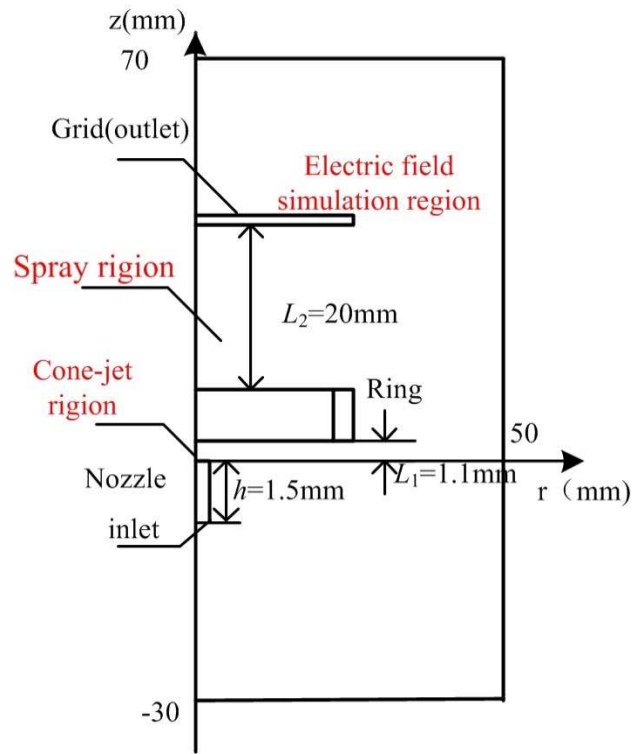
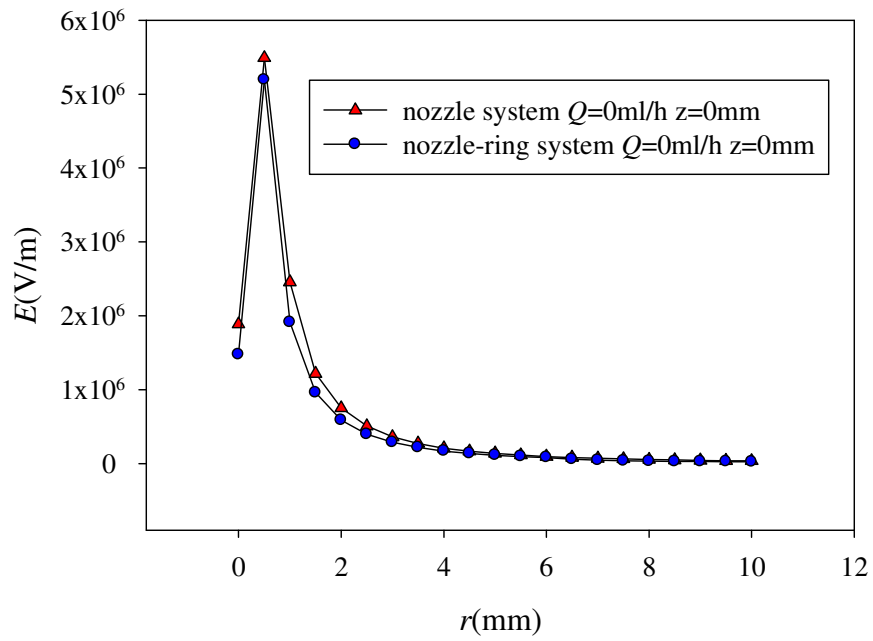
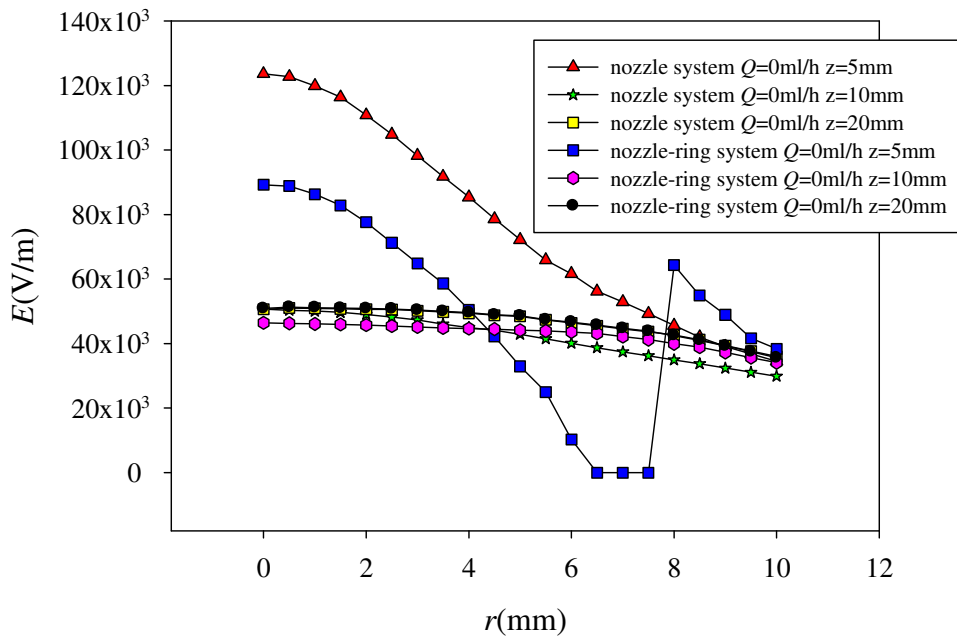


Fig.4 Geometric model of numerical simulation

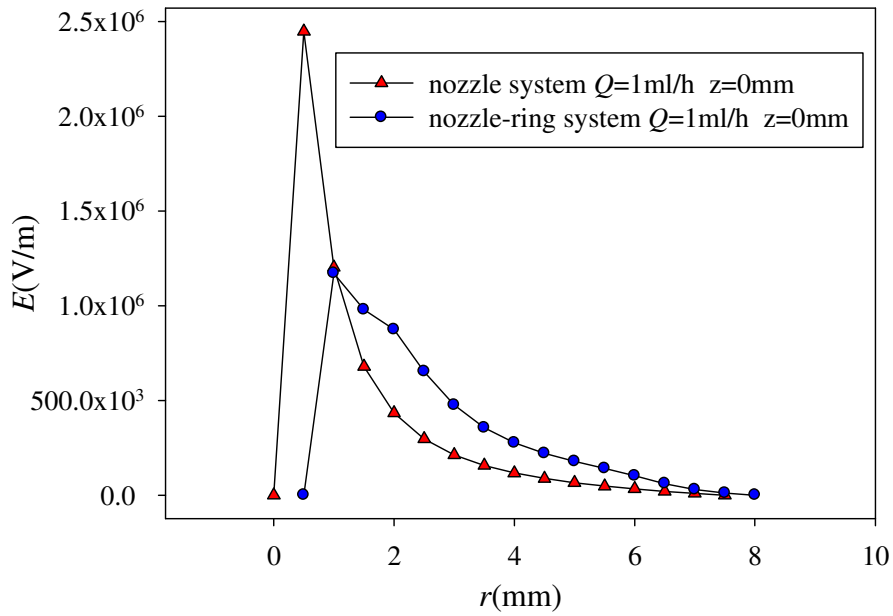


(a) at the cone-jet region

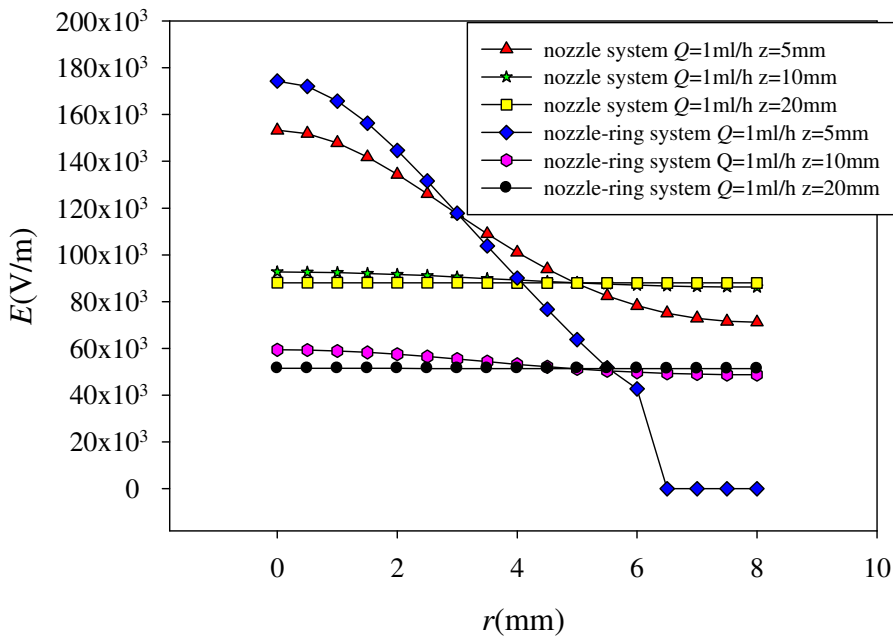


(b) at the spraying region

Fig.5 Electric field distributions at cone-jet region and spraying region without fuel



(a) at the cone-jet region



(b) at the spraying region

Fig.6 Electric field distributions at cone-jet region and spraying region with fuel

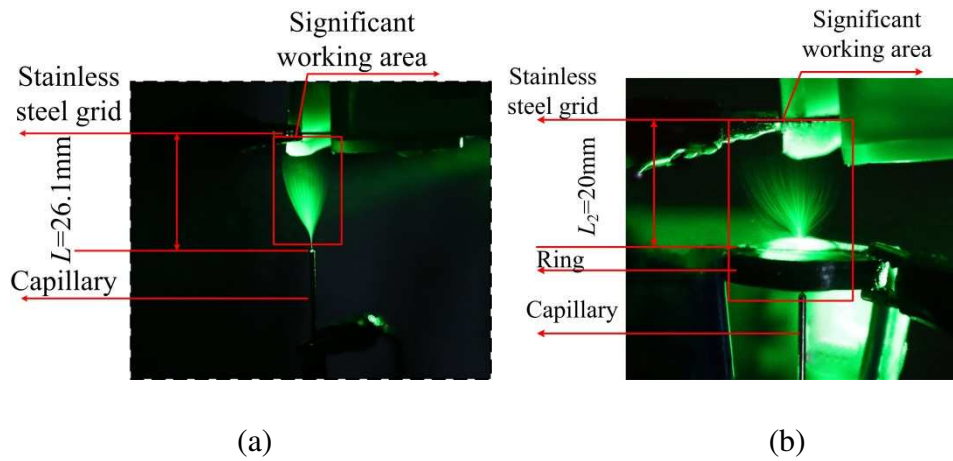
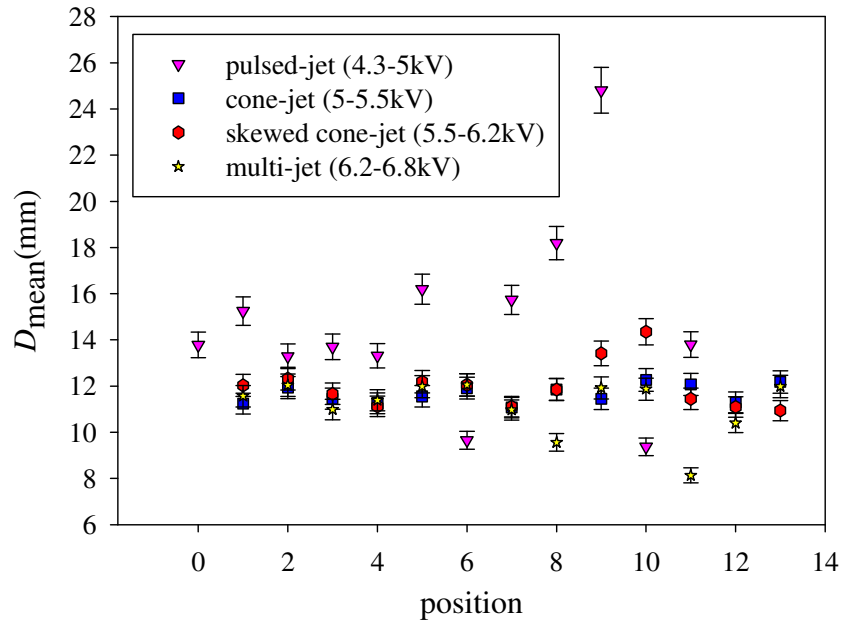


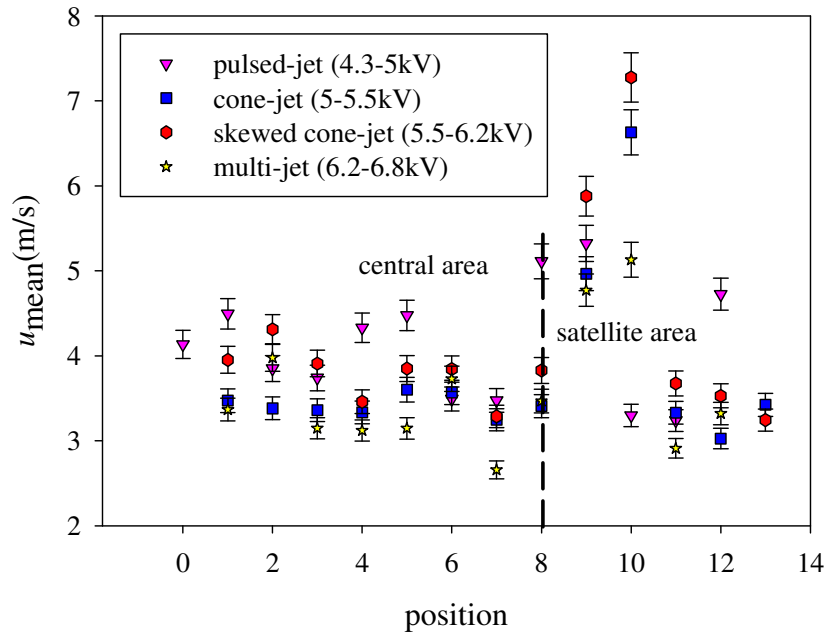
Fig.7 Typical images of the electro-spraying at the two different systems

(a) nozzle system ($L=26.1$ mm, $V_n=5.2$ kV, $Q=1.0$ ml/h)

(b) nozzle-ring system ($L_1=1.1$ mm, $L_2=20$ mm, $V_n=4.2$ kV, $V_r=1$ kV, $Q=1.0$ ml/h)

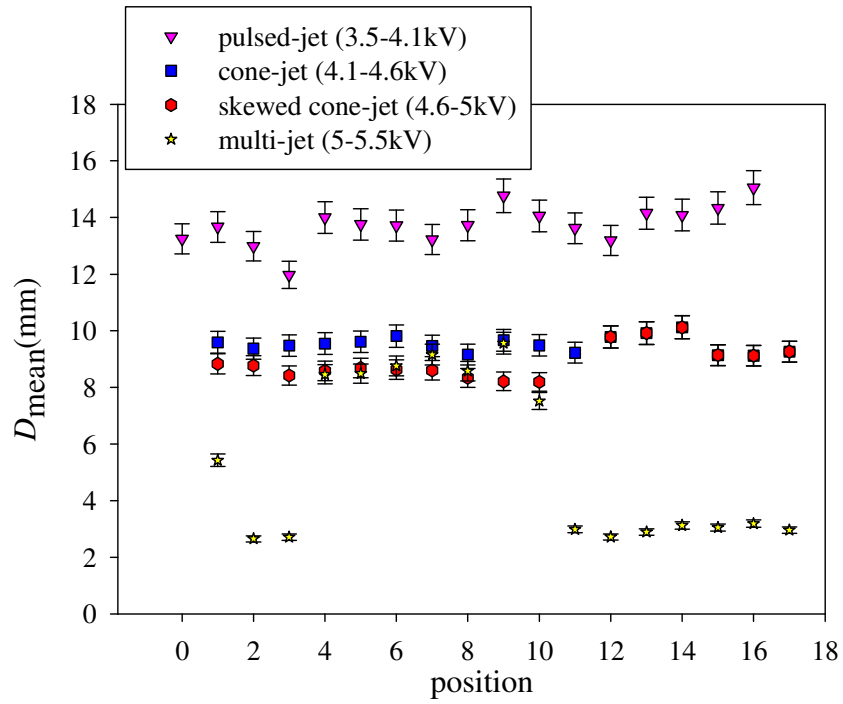


(a) Droplet size distribution for nozzle system at different modes and positions

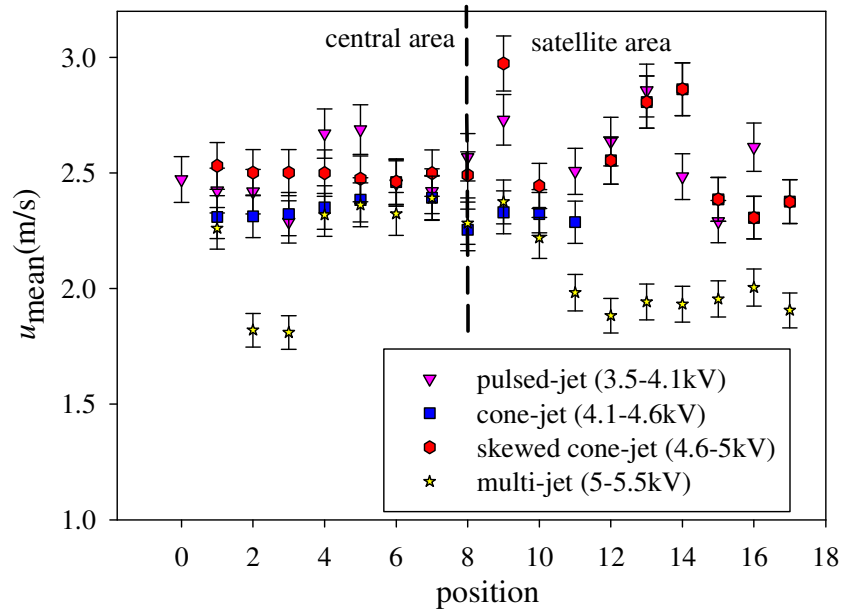


(b) Droplet velocity distribution for nozzle system at different modes and positions

Fig.8 Droplet size and velocity distributions for nozzle system at different modes and positions ($L=26.1$ mm, $z=10$ mm, $Q=1$ ml/h)



(a) Droplet size distribution for nozzle-ring system at different modes and positions



(b) Droplet velocity distribution for nozzle-ring system at different modes and positions

Fig.9 Droplet size and velocity distributions for nozzle-ring system at different modes

and positions ($L_1=1.1$ mm, $L_2=20$ mm, $z=10$ mm, $V_2=1$ kV, $Q=1$ ml/h)

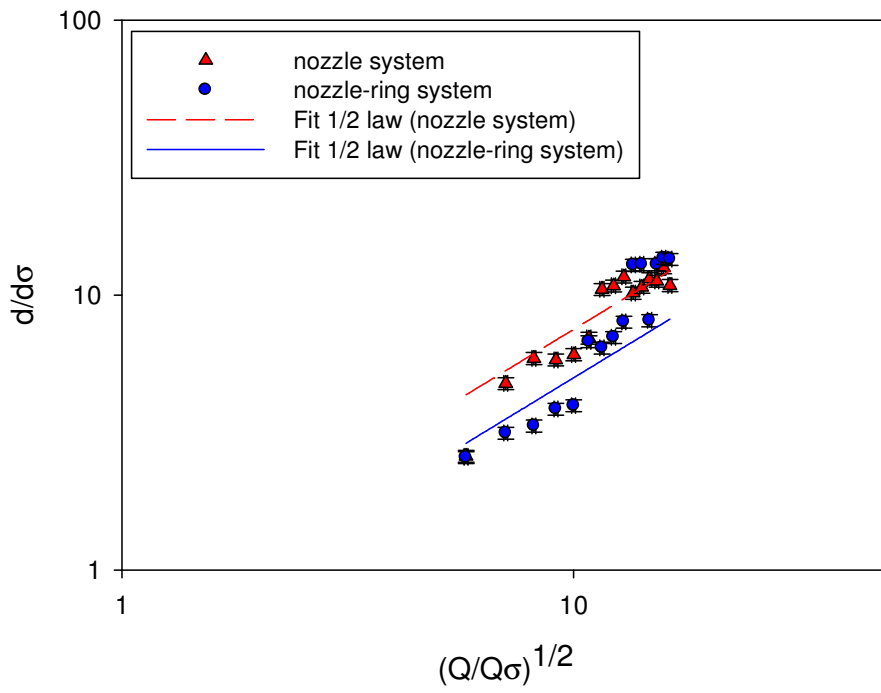


Fig.10 Dimensionless average droplet size versus dimensionless average flow rate at cone-jet mode